

TURKISH JOURNAL OF REMOTE SENSING
(Türkiye Uzaktan Algılama Dergisi)
e-ISSN 2687-4997
https://dergipark.org.tr/en/pub/tuzal

Topographic heterogeneity and long-term vegetation dynamics in a humid mountain landscape: Evidence from a Shannon entropy-based framework

Fatih Işık[*1]

[1] *Gümüşhane University, Faculty of Literature, Department of Geography, Gümüşhane, Türkiye;* isikfatih@gumushane.edu.tr

Check for updates

Article History:
Received: 5 May 2026
Revised: 6 July 2026
Accepted: 9 July 2026
Published: 5 October 2026

Copyright: © 2026 by the author.
This article is an open access article distributed under terms and conditions of the Creative Commons Attribution (CC BY-SA) license. https://creativecommons.org/licenses/by-sa/4.0/

Abstract: Topographic heterogeneity can mediate radiation, moisture redistribution, and microclimate, yet it is commonly represented by single terrain variables. We evaluated long-term vegetation dynamics across low, moderate, and high topographic heterogeneity (TH) classes in Trabzon, northeastern Türkiye, using a 5 m-grid Shannon entropy-based Topographic Heterogeneity Index (THI), Landsat NDVI/EVI (1985–2025), CORINE land cover, elevation strata, and TerraClimate PDSI (1985–2024). High TH maintained higher mean productivity than low TH, with a larger contrast for EVI (32.3%) than NDVI (9.8%); differences were strongest below 2000 m and converged at higher elevations. All classes greened significantly, although the moderate class showed the largest trend magnitude, whereas high TH showed lower relative temporal variability. After controlling class-specific temporal trends and clustering inference by year, current-year PDSI effects were not supported. Previous-year PDSI slopes differed among TH classes; the only individually significant slope was a negative EVI association in low TH ($\beta = -0.00524$, $p = 0.0167$), while NDVI class-specific slopes were not significant. Trend-adjusted drought metrics showed event-specific responses rather than a uniform drought-year decline; recovery and resilience ratios remained above 1 but were based on four events. A raster-scale sensitivity analysis retained 77.5% agreement with the 5 m classification at 30 m ($\kappa = 0.586$), declining to 72.0% at 100 m ($\kappa = 0.468$). The results support a robust association of terrain complexity with vegetation productivity and relative stability, while emphasizing limits related to spatial scale and regional drought indices.

Keywords: Topographic heterogeneity; NDVI; EVI; hydroclimatic lag; scale sensitivity

Citation: Işık, F. (2026). Topographic heterogeneity and long-term vegetation dynamics in a humid mountain landscape: Evidence from a Shannon entropy-based framework. *Turk. J. Remote Sens.*, 8, 1944988. https://doi.org/10.51489/tuzal.1944988

1. Introduction

Terrestrial vegetation dynamics are shaped by the interaction of climate, land cover, disturbance regimes, and the physical structure of the landscape (Sturtevant & Fortin, 2021). Remote sensing has made it possible to monitor these dynamics over multi-decadal periods, with vegetation indices such as the Normalized Difference Vegetation Index (NDVI) and Enhanced Vegetation Index (EVI) widely used as proxies for vegetation greenness, productivity, and canopy condition (Huete et al., 2002; Tucker, 1979). However, long-term vegetation variability is often interpreted primarily through broad-scale climatic gradients or land-use change, whereas the role of terrain structure as a spatial filter of vegetation processes remains less explicitly quantified (Liang et al., 2024). This is a critical limitation in mountainous and dissected landscapes, where topography mediates solar radiation, soil moisture, wind exposure, cold-air drainage, and local hydroclimatic conditions over short distances (Moeslund et al., 2013; Stein et al., 2014). Topography therefore does not merely provide a background template for vegetation; it can actively structure the spatial distribution, productivity, and temporal variability of plant communities (Işık & Eraslan, 2026).

Topographic heterogeneity refers to the structural diversity of terrain conditions, including variation in elevation, slope, aspect, surface roughness, landform position,

radiation exposure, and moisture redistribution (J. Wang et al., 2023). This concept differs from land-cover heterogeneity, which describes the composition and configuration of surface-cover classes. While land-cover heterogeneity reflects the current ecological or anthropogenic surface state, topographic heterogeneity represents a more persistent physiographic framework that can influence the conditions under which vegetation develops. Previous work has shown that environmental and topographic heterogeneity can increase niche availability, generate microclimatic gradients, support local diversity patterns, and mediate ecological responses to regional climate change (Moeslund et al., 2013; Suggitt et al., 2018). In mountain landscapes, such heterogeneity can create fine-scale variation in vegetation response, even when regional climate forcing is shared across the broader landscape (Bueno de Mesquita et al., 2018).

Despite this recognized importance, topographic heterogeneity is frequently simplified in vegetation studies. Many analyses represent terrain using single variables such as elevation, slope, aspect, or ruggedness (Liang et al., 2024). Although these variables are informative, they capture only one component of terrain complexity and may fail to represent the multidimensional structure of the landscape. This is particularly problematic in regions where several topographic controls operate simultaneously. Aspect can modify radiation exposure, valley–ridge position can influence moisture accumulation and exposure, and surface roughness can generate local variability in habitat conditions (Wani et al., 2023). A single topographic metric cannot adequately capture this combined variability. Information-theory approaches, particularly Shannon entropy, provide a useful framework for quantifying heterogeneity because they measure the diversity and proportional representation of categorical states within a defined neighborhood (Shannon, 1948; C. Wang & Zhao, 2018). Applied to terrain derivatives, this approach allows topographic heterogeneity to be represented as a composite landscape property rather than as an isolated terrain variable.

Türkiye provides a particularly relevant geographical setting for this problem. Its position between major biogeographic regions, high mountain systems, and strong environmental gradients has produced high biological and physiographic diversity (Kaya & Raynal, 2001; Şekercioğlu et al., 2011). In such landscapes, vegetation patterns may be influenced not only by climate and land cover, but also by the underlying diversity of terrain structure. The Eastern Black Sea region is especially suitable for testing this relationship because steep elevation gradients, humid climatic conditions, and extensive vegetation cover occur over short horizontal distances (Gürçay et al., 2025; Işık et al., 2024). Trabzon Province was therefore selected as a pilot mountainous landscape in which the relevance of high-resolution topographic heterogeneity for long-term vegetation dynamics could be evaluated. Recent regional evidence from the Eastern and Central Black Sea also shows that elevation, slope, and aspect strongly structure the spatial distribution of human modification, reinforcing the need to account for topographic controls when interpreting vegetation and land-cover patterns in this region (Eraslan, 2024).

A key gap remains in understanding whether multidimensional topographic heterogeneity is associated with vegetation productivity, temporal stability, and hydroclimatic sensitivity after accounting for elevation and land-cover structure (Ibarra-Manríquez et al., 2022; Muscarella et al., 2020; Xu et al., 2015). Existing studies have often focused on single terrain variables, short-term vegetation responses, or broad climatic controls, while fewer studies have combined high-resolution terrain heterogeneity metrics with multi-decadal satellite-derived vegetation records (Torresani et al., 2024). Addressing this gap is important because topographic heterogeneity may help explain why vegetation productivity and variability differ among areas exposed to similar regional climatic conditions.

The aim of this study is to evaluate how topographic heterogeneity relates to long-term vegetation dynamics in a humid mountainous landscape. Rather than treating topography as

a single elevation or slope variable, this study uses a multidimensional topographic heterogeneity framework and links it with long-term NDVI and EVI records, land-cover information, elevation zones, and hydroclimatic variability. Specifically, the study addresses three research questions:

(1) Do low, moderate, and high topographic heterogeneity classes differ in long-term NDVI and EVI productivity after accounting for elevation and land-cover structure?
(2) Do vegetation indices show different long-term trends and interannual stability across topographic heterogeneity classes?
(3) Does topographic heterogeneity modify vegetation responses to current and lagged hydroclimatic variability and to objectively selected extreme drought years?

Based on the role of terrain complexity in structuring local environmental conditions, we expected that areas with higher topographic heterogeneity would show higher vegetation productivity and lower interannual variability than areas with lower heterogeneity. However, we also expected that these relationships could vary between NDVI and EVI because the two indices differ in their sensitivity to canopy structure and high-biomass vegetation conditions. By shifting the focus from individual terrain variables to a multidimensional, entropy-based measure of topographic complexity, this study provides a transferable framework for evaluating the relationship between terrain structure and vegetation dynamics in mountainous landscapes.

2. Materials and Methods

2.1. Study area

The study was conducted in Trabzon Province in the northeastern Black Sea region of Türkiye (40°30′–41°30′ N, 38°30′–40°30′ E), covering approximately 4664 km^2 (Figure 1). The province is a humid mountain landscape with relief rising from sea level to more than 3400 m within less than 50 km. The climate is humid temperate (Köppen Cfb), and annual precipitation exceeds 2000 mm in high-altitude sectors (Öztürk et al., 2017). The elevation gradient supports deciduous forests below approximately 800 m, mixed and coniferous forests dominated locally by *Picea orientalis* between about 800 and 2000 m, and alpine vegetation above the treeline (>2000 m) (Atalay, 2002). Vegetation indices were analyzed for 1985–2025; Palmer Drought Severity Index (PDSI)-based analyses covered 1985–2024.

2.2. Overall workflow

The research followed a multi-scale integrative framework linking terrain complexity with multi-decadal vegetation dynamics. The methodological pipeline consisted of four interconnected stages (Figure 2):

Topographic Heterogeneity Modeling: A fine-grid Topographic Heterogeneity Index (THI) was produced in SAGA GIS v9.8.1 from 11 terrain-derived layers using local Shannon entropy (Conrad et al., 2015).

Stratification and Classification: The archived 0–5 THI class raster was regrouped as low (0–1), moderate (2), and high (3–5) heterogeneity. The upper classes were merged to avoid sparse strata while retaining the upper tail of terrain complexity.

Big Data Processing in Google Earth Engine (GEE): A stratified data extraction was performed using GEE (Gorelick et al., 2017). Landsat-derived NDVI and EVI composites (1985–2025) were intersected with a unique ClassID layer, formed by the spatial overlay of land-cover × elevation × THI units. NDVI was selected to monitor chlorophyll-sensitive greenness (Aktaş, 2024), while EVI was integrated to minimize atmospheric noise and account for structural canopy variations in high-biomass areas (Huete et al., 2002).

Statistical Synthesis and Robustness Testing: Annual April–October summaries were analyzed in R v4.2.2 using area weights. Hydroclimatic models incorporated class-specific

temporal trends, current- and previous-year PDSI, and year-clustered bias-reduced cluster-robust (CR2) inference. Drought metrics were recalculated after temporal detrending, and an independent raster-scale sensitivity analysis evaluated the stability of topographic heterogeneity (TH) classes at 30 and 100 m.

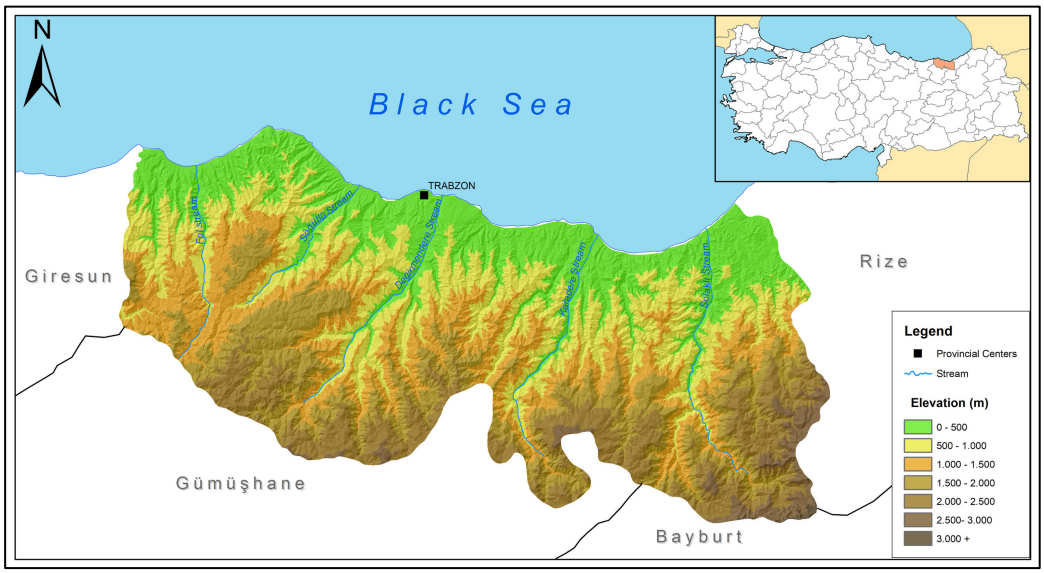


Figure 1. Location of Trabzon Province in northeastern Türkiye

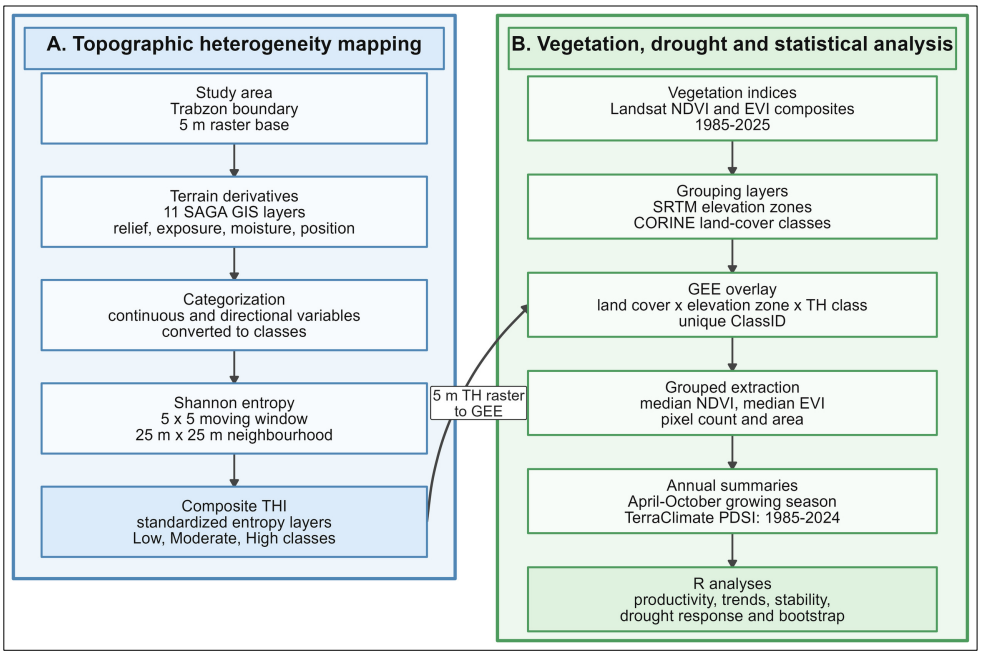


Figure 2. Overall methodological workflow used to link topographic heterogeneity with long-term vegetation dynamics

2.3. Topographic data and heterogeneity mapping

The archived THI product used in this study is a single-band raster with 5 m output cell spacing in Universal Transverse Mercator (UTM) Zone 37N (EPSG:32637). The original terrain-processing archive did not retain the provenance of the source elevation model; consequently, 5 m is reported strictly as the output grid spacing of the THI and not as verified native digital elevation model (DEM) accuracy. This metadata limitation is explicitly considered when interpreting fine-scale patterns.

Eleven terrain-derived layers were processed in SAGA GIS v9.8.1 (Conrad et al., 2015) to represent morphometry (elevation, slope, ruggedness, and roughness), hydro-

geomorphology (topographic moisture, flow-related terrain, and topographic position), energy exposure (solar radiation and hillshade), and orientation (aspect and aspect suitability). Together, these layers describe complementary controls on relief, water redistribution, exposure, and terrain position (Figure 3; Riley et al., 1999; Weiss, 2001).

Continuous layers were discretized into categorical states, and directional variables were grouped by orientation. Local Shannon entropy was calculated in a 5 × 5-cell moving window. Because the output grid spacing was 5 m, the nominal neighborhood was 25 × 25 m, close to the spatial grain of Landsat observations. Shannon entropy was calculated using Eq. (1):

$$H' = -\sum_{i=1}^{S} p_i \ln(p_i) \quad (1)$$

where S is the number of terrain states in the moving window and p_i is the proportional abundance of state i. The 11 entropy layers were standardized before combination so that layers measured on different numerical ranges contributed on a comparable scale, and the standardized layers were combined with equal weights using Eq. (2). Equal weighting was selected because the layers represent complementary terrain dimensions and no independently validated ecological basis was available for assigning differential weights.

$$THI = \frac{1}{n}\sum_{j=1}^{n} H'_{j,standardized}, n = 11 \quad (2)$$

The equal-weight formulation assumes comparable ecological relevance among standardized layers and does not explicitly remove inter-layer correlation. A principal component analysis (PCA)-weighted index could reduce covariance and maximize explained statistical variance, but its loadings would be sample-specific and variance-based rather than direct measures of ecological importance. Accordingly, equal weighting was retained for interpretability, and the absence of a PCA-weighted sensitivity analysis is acknowledged as a limitation. The archived 0–5 raster was regrouped into low (0–1), moderate (2), and high (3–5) TH classes.

2.4. Cloud-based data extraction and spatial integration

Long-term vegetation dynamics were analyzed using the GEE platform, which enables high-performance processing of multi-decadal satellite archives (Gorelick et al., 2017). We utilized Landsat Collection 2 Tier 1 Level 2 (Surface Reflectance) data, which provides the highest radiometric quality and consistent cross-calibration across the Landsat 5, 7, 8, and 9 sensors (Masek et al., 2020).

Two primary vegetation indices were extracted to capture complementary aspects of plant productivity:

NDVI: NDVI = (NIR − Red)/(NIR + Red), used as a proxy for chlorophyll-sensitive greenness and photosynthetic capacity (Tucker, 1979).

EVI: EVI = 2.5 × (NIR − Red)/(NIR + 6Red − 7.5Blue + 1), designed to reduce atmospheric and canopy-background effects in dense vegetation (Huete et al., 2002).

Monthly 32-day NDVI and 8-day EVI composites were summarized for the April–October growing season. Elevation zones were derived from the 30 m United States Geological Survey (USGS) Shuttle Radar Topography Mission (SRTM) v3 DEM and classified as 0–250, 250–500, 500–750, 750–1000, 1000–1500, 1500–2000, 2000–3000, and >3000 m (Farr et al., 2007).

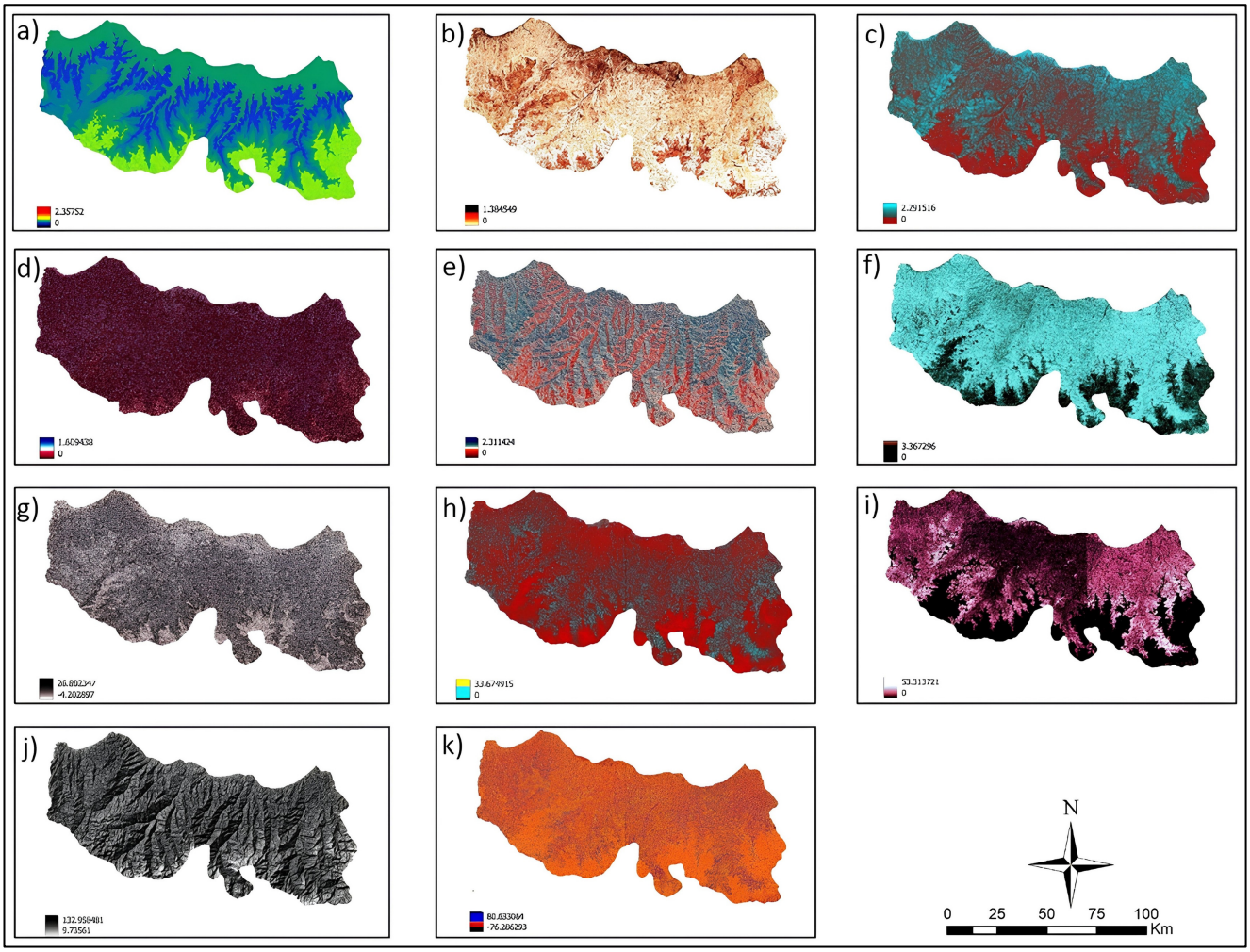


Figure 3. Terrain-derived Shannon entropy layers used in the construction of the Topographic Heterogeneity Index. Panels show Shannon entropy surfaces for (a) elevation, (b) slope, (c) aspect, (d) flow-related terrain layer, (e) aspect suitability, (f) solar radiation index, (g) topographic moisture, (h) ruggedness, (i) roughness, (j) hillshade, and (k) topographic position index

Temporal land-cover changes were controlled using the Copernicus Coordination of Information on the Environment (CORINE) land-cover dataset (100 m). We applied a temporal synchronization rule, where each Landsat observation year was matched with the chronologically closest CORINE layer (1990, 2000, 2006, 2012, or 2018). To ensure the analysis focused on ecological productivity, non-vegetated classes (urban, artificial surfaces, and water bodies) were strictly excluded (Büttner, 2014).

The THI asset, SRTM elevation zones, and temporally matched CORINE land-cover classes were combined categorically to generate a ClassID for grouped extraction using Eq. (3). The retained analytical table records valid 30 m Landsat pixel counts, and analysis areas were therefore based on realized Landsat observations. CORINE was used only as a categorical thematic stratum; assigning its classes to the analytical grid did not increase the native 100 m information content. Accordingly, 5 m refers only to the THI output grid spacing, not to the resolution of the vegetation analysis.

$$ClassID = (LC \times 100) + (EZ \times 10) + TH \quad (3)$$

where LC is the CORINE land-cover code, EZ is the elevation-zone code, and TH is the three-class topographic heterogeneity code. The identifier supported grouped extraction of median NDVI/EVI values, valid pixel counts, and analysis area.

2.5. Vegetation index summarization and area estimation

The data extraction in GEE was initially conducted for an extended phenological window (March to November). However, to minimize the potential interference of late-spring snow cover and low solar zenith angles in the high-altitude zones of the Eastern Black Sea Mountains, the final statistical summaries were restricted to the core growing season, defined as April to October. This window ensures that the captured signal represents peak photosynthetic activity and stable leaf-on conditions in temperate mountain forests (White et al., 2009).

Spatial summaries were generated with ee.Reducer.median().group(). The median was used to reduce sensitivity to residual cloud contamination, terrain-shadow outliers, and sensor artifacts (Flood, 2013). For each ecological unit u, the valid analysis area was calculated from the number of unmasked Landsat pixels using Eq. (4):

$$A_u = N_u \times (30\,m \times 30\,m) = N_u \times 0.0009\,\mathrm{km}^2 \quad (4)$$

where N_u is the valid Landsat pixel count. Area weighting therefore reflected the realized, cloud-masked vegetation surface rather than theoretical class extent.

2.6. Regional hydroclimatic forcing: TerraClimate PDSI

To evaluate the influence of interannual moisture variability on vegetation dynamics, we utilized the PDSI from the TerraClimate dataset (Abatzoglou et al., 2018). TerraClimate provides high-temporal resolution (monthly) water-balance variables by integrating high-spatial-resolution climatological averages (WorldClim) with coarser-resolution time-series data (Climatic Research Unit (CRU) TS4.0 and Japanese 55-year Reanalysis (JRA-55)), making it uniquely suited for long-term ecological studies in complex terrains where station-based data are sparse.

The PDSI was selected because it accounts for both precipitation and evapotranspiration, providing a comprehensive measure of cumulative moisture surplus or deficit. The data were extracted via GEE at a spatial resolution of 1/24° (~4 km). Following the dataset's metadata, a scale factor of 0.01 was applied to the raw values. For each year, a mean growing-season PDSI was calculated by averaging monthly values from April to October.

It is important to note that PDSI was employed as a regional hydroclimatic indicator representing macroclimatic pulses rather than a local microclimatic measurement. This approach allows for the assessment of how high-resolution topographic heterogeneity mediates the vegetation response to broader regional climate fluctuations. Due to the temporal availability of the TerraClimate archive at the time of analysis, the climate-sensitivity and drought-response models covered the period 1985–2024, whereas the autonomous vegetation trend analyses extended to 2025.

2.7. Statistical analyses

Statistical analyses were performed in R v4.2.2 (R Core Team, 2022). NDVI and EVI values outside −1 to 1 were excluded. Monthly observations were aggregated into year × land-cover × elevation-zone × TH-class ecological units, with at least three valid growing-season months required. This aggregation reduced pixel-level pseudo-replication, but it did not guarantee removal of residual spatial dependence.

Area-weighted annual means were used to compare productivity among TH classes. Monotonic trends were evaluated using the Mann–Kendall test and Sen's slope (Mann, 1945; Sen, 1968). Temporal variability was summarized using the coefficient of variation [Eq. (5)] and deviations from each unit's long-term mean [Eq. (6)].

Extreme drought candidates were defined as years in the lowest 10% of growing-season PDSI. Consecutive candidate years were treated as a single event cluster, represented by the year with the minimum PDSI. Resistance [Eq. (8)], recovery [Eq. (9)], and resilience [Eq. (10)]

used two-year pre-event and two-year post-event windows. To prevent long-term greening from inflating post-drought ratios, annual NDVI and EVI series were divided by their class-specific fitted temporal trends [Eq. (7)]; linear detrending was used for the primary results, with quadratic and natural-cubic-spline trends as sensitivity checks.

$$CV_u = 100 \times \frac{\mathrm{SD}(VI_{u,t})}{\mathrm{Mean}(VI_{u,t})} \tag{5}$$

$$\mathrm{Anomaly}_{u,t} = VI_{u,t} - \mathrm{Mean}(VI_u) \tag{6}$$

$$VI_{\mathrm{adjusted,t}} = \frac{VI_{\mathrm{observed,t}}}{VI_{\mathrm{expected\ trend,t}}} \tag{7}$$

$$\mathrm{Resistance} = \frac{VI_{\mathrm{drought}}}{\mathrm{Mean}(VI_{\mathrm{pre}})} \tag{8}$$

$$\mathrm{Recovery} = \frac{\mathrm{Mean}(VI_{\mathrm{post}})}{VI_{\mathrm{drought}}} \tag{9}$$

$$\mathrm{Resilience} = \frac{\mathrm{Mean}(VI_{\mathrm{post}})}{\mathrm{Mean}(VI_{\mathrm{pre}})} \tag{10}$$

Regional hydroclimatic sensitivity was re-evaluated on a common 1986–2024 sample using current-year PDSI, previous-year PDSI, and a combined current-plus-lag model. Because each annual PDSI value was repeated across ecological units, coefficient inference used CR2 standard errors clustered by year. The primary lagged model included class-specific linear time trends, elevation, and land cover, as specified in Eq. (11):

$$\begin{aligned}\mathrm{Anomaly}_{u,t} = {} & \beta_0 + \beta_{1\mathrm{PDSI}_{t-1}} + \beta_{2TH_u} + \beta_{3(\mathrm{PDSI}_{t-1} \times TH_u)} + \beta_4 \mathrm{Year}_t + \beta_5(\mathrm{Year}_t \times TH_u) + \beta_6 Elevation_u \\ & + \beta_7 LandCover_u + \varepsilon_{u,t}\end{aligned} \tag{11}$$

Joint PDSI × TH interactions were evaluated with year-clustered CR2 Wald tests. Akaike information criterion (AIC) and Bayesian information criterion (BIC) were used only as secondary model-comparison criteria because the effective hydroclimatic replication was 39 years. Robustness was assessed by replacing linear class-specific trends with quadratic and natural cubic spline (df = 3) trends. A separate stratified bootstrap (1000 iterations) resampled matched year × elevation × land-cover High–Low contrasts to evaluate productivity differences (Efron & Tibshirani, 1994).

3. Results

3.1. Spatial patterns of topographic heterogeneity and vegetation productivity

The spatial distribution of topographic heterogeneity and vegetation productivity reveals marked geographic variation across Trabzon Province (Figure 4). The topographic heterogeneity map (Figure 4a) highlights the fragmented terrain structure of the Eastern Black Sea Mountains, where higher heterogeneity values are mainly concentrated along deeply incised valleys, rugged hillslopes, and mid-altitudinal mountain belts.

A visual comparison between topographic heterogeneity and the long-term mean NDVI and EVI patterns suggests a clear spatial correspondence between terrain complexity and vegetation productivity (Figure 4b,c). Areas characterized by higher topographic heterogeneity generally coincide with zones of relatively high greenness, particularly along central and coastal-facing slopes. This pattern may reflect the combined influence of local moisture accumulation, slope-driven microclimate variation, topographic shading, and habitat diversity on vegetation development.

The representative field photographs taken from the marked area in Figure 4a provide ground-level context for these spatial patterns (Figure 4d–f). The photographs illustrate rugged terrain, exposed rock surfaces, steep hillslopes, and heterogeneous vegetation structure, all of which are consistent with the high terrain complexity captured by the topographic heterogeneity index. These initial spatial observations provide a basis for the subsequent quantitative analyses of vegetation productivity across topographic heterogeneity, elevation, and land-cover gradients.

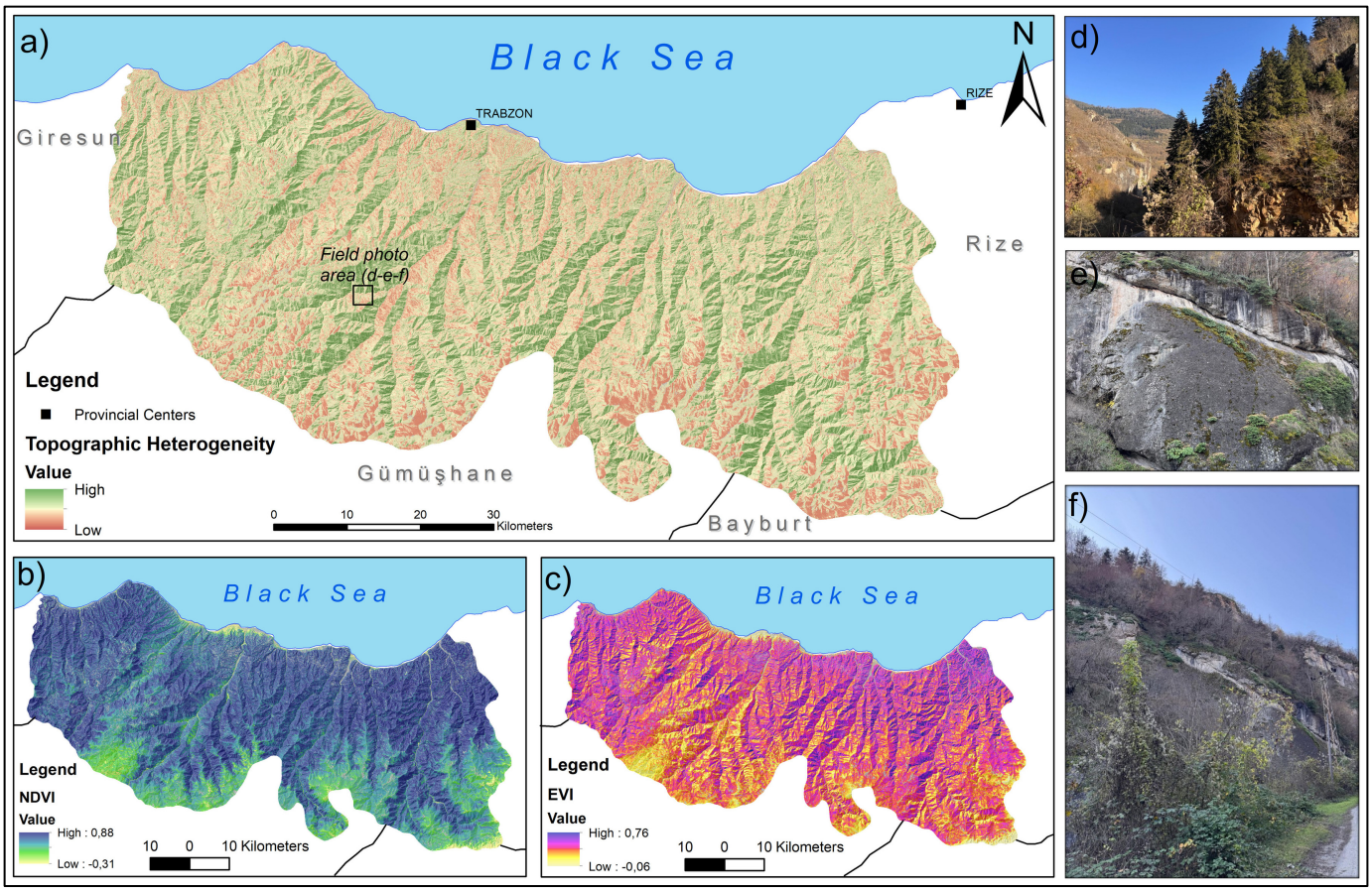


Figure 4. Spatial distribution of (a) topographic heterogeneity, (b) long-term mean NDVI, and (c) long-term mean EVI across Trabzon Province. The black rectangle in panel (a) indicates the representative field-photo area. Panels (d–f) show field photographs from this area, illustrating rugged hillslopes, exposed rock surfaces, and heterogeneous vegetation structure associated with complex terrain conditions

3.2. Altitudinal distribution of topographic heterogeneity classes

The proportional representation of TH classes exhibited non-linear variations across the altitudinal gradient of the study area (Figure 5). The moderate heterogeneity class constituted the dominant physiographic matrix in all elevation belts, consistently accounting for more than 50% of the total area. This dominance was most pronounced in the montane (1500–2000 m) and high-alpine (3000+ m) zones, where terrain complexity remained relatively uniform.

The high heterogeneity class followed a distinct unimodal distribution, occupying a substantial proportion (approximately 30–35%) of the landscape within the lower and middle elevation zones (0–1500 m). The maximum relative share of high TH was observed in the 1000–1500 m belt, indicating peak terrain fragmentation in this transitional zone. Above 1500 m, the share of high heterogeneity decreased sharply, reaching its minimum at the highest altitudes (>3000 m).

In contrast, the low heterogeneity class remained a minority (typically <20%) across most zones below 2000 m. However, a significant expansion of low TH areas was observed in the high-alpine regions (2000–3000 m and >3000 m), where high-altitude plateaus and smoother summit reliefs became more prevalent. These findings demonstrate that the physical template for vegetation development—defined by topographic complexity—is stratigraphically organized along the elevation gradient.

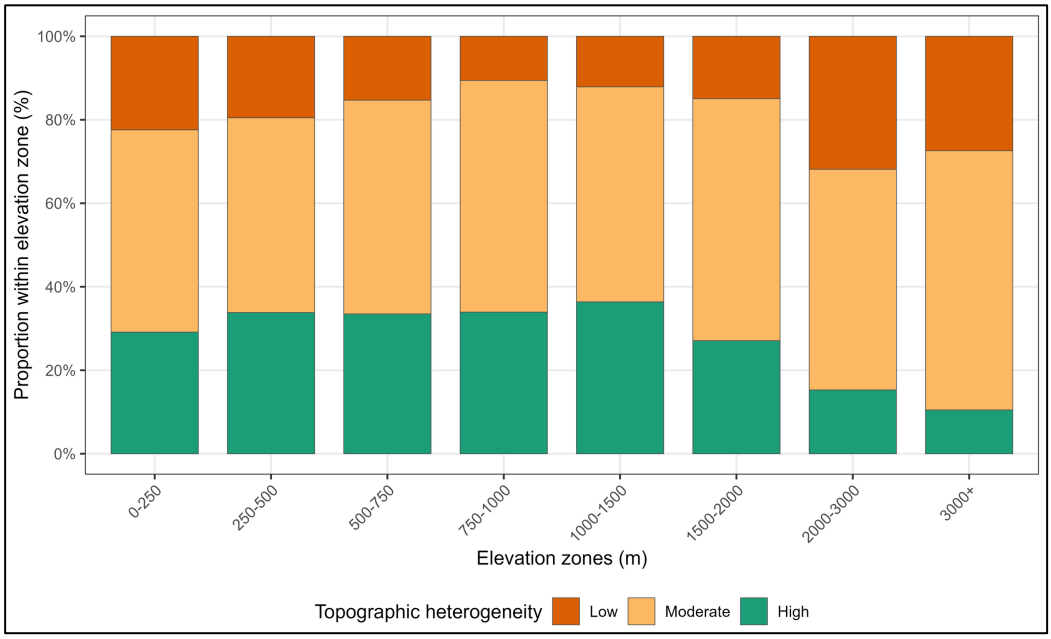


Figure 5. Area-based distribution of topographic heterogeneity classes across elevation zones. Percentages represent the proportional area of low, moderate, and high topographic heterogeneity classes within each elevation zone. Area values were calculated in km^2

3.3. Area-weighted NDVI and EVI productivity across topographic heterogeneity classes

The area-weighted annual growing-season NDVI and EVI values exhibited systematic variations across the TH gradient (Figure 6). For both indices, a positive monotonic relationship was observed, with mean values increasing from the low to the high heterogeneity class.

For NDVI, the area-weighted mean values were recorded as 0.662 for the low class, 0.701 for the moderate class, and 0.727 for the high heterogeneity class (Figure 6B). Violin plots indicated a substantial distributional overlap between the three categories; however, the high TH class consistently maintained the highest central tendency. The 95% confidence intervals (CIs) for the mean values remained narrow across all classes, indicating high precision in the area-weighted estimates.

The magnitude of difference was more pronounced for EVI than for NDVI. Mean EVI values increased from 0.371 (low class) and 0.413 (moderate class) to 0.491 in the high heterogeneity class. Unlike NDVI, the EVI distribution for high TH areas showed a distinct upward shift relative to the low and moderate classes (Figure 6A). The relative increase in mean productivity from low to high heterogeneity was approximately 9.8% for NDVI and 32.3% for EVI, indicating a sharper contrast in structural greenness than in chlorophyll-sensitive greenness across the terrain complexity gradient.

3.4. Altitudinal stratification of NDVI and EVI across heterogeneity classes

The interaction between elevation and TH resulted in distinct productivity patterns across the altitudinal gradient (Figure 7). While both indices showed a general decline with increasing altitude, the influence of TH was non-uniform across different zones.

NDVI patterns: In the lower-to-middle elevation zones (0–1000 m), NDVI remained high (approximately 0.74–0.78) with limited inter-class separation. Differences widened between 1000 and 2000 m; in the 1500–2000 m belt, high TH retained a mean NDVI of 0.708 compared with 0.653 for moderate and 0.627 for low TH. Above 2000 m, NDVI declined sharply and class differences narrowed, reaching the lowest values above 3000 m.

EVI patterns: EVI showed clearer separation among TH classes from sea level to 2000 m. In the 250–500 m belt, mean EVI was 0.417, 0.467, and 0.558 in low, moderate, and high TH, respectively. This ordering persisted through 1500–2000 m. Above 2000 m, EVI converged rapidly (0.322–0.353 in the 2000–3000 m belt); above 3000 m, all classes showed strong productivity limitation.

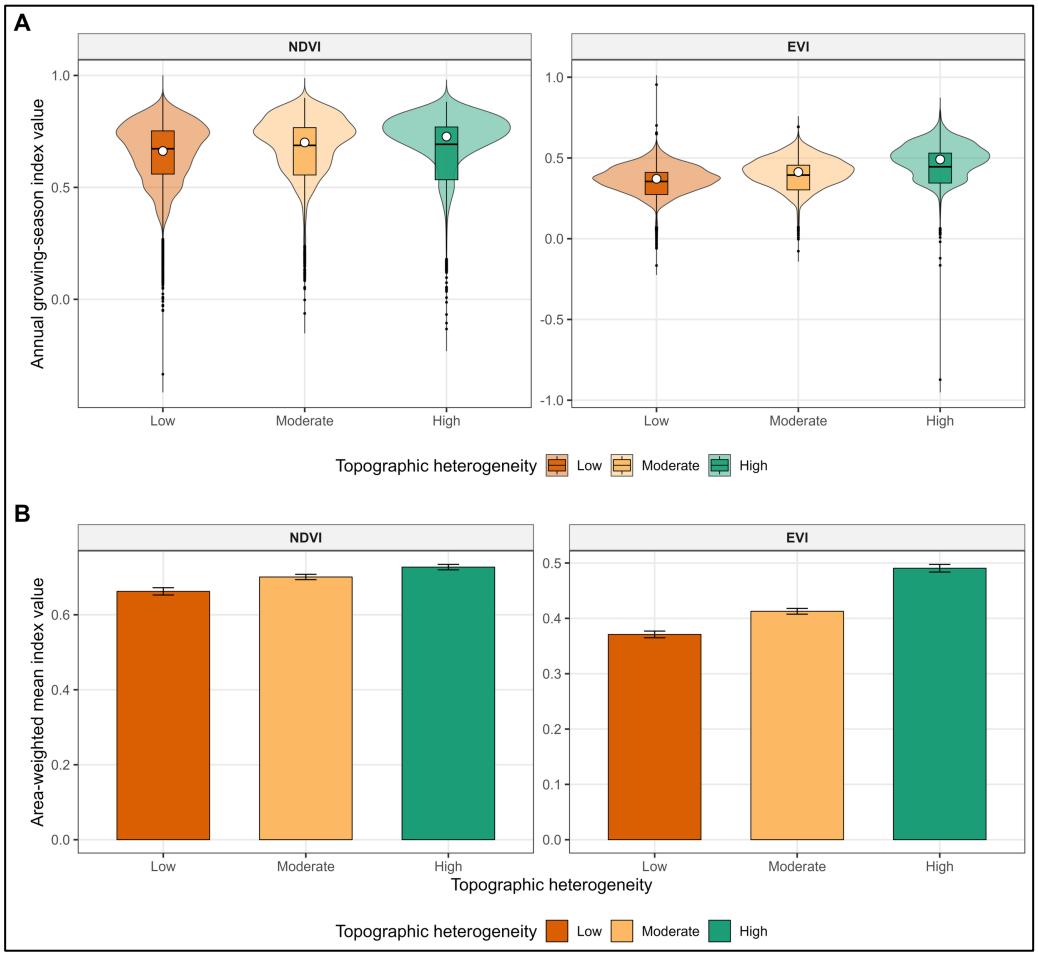


Figure 6. Area-weighted NDVI and EVI productivity across topographic heterogeneity classes. (A) Distribution of annual growing-season NDVI and EVI unit means across low, moderate, and high topographic heterogeneity classes. (B) Area-weighted mean NDVI and EVI values with 95% confidence intervals. White points indicate area-weighted class means

3.5. Long-term NDVI and EVI trends across topographic heterogeneity classes

Area-weighted annual growing-season NDVI and EVI increased monotonically in all TH classes during 1985–2025 (Figure 8; Table 1). All Mann–Kendall tests and Sen-slope estimates were positive ($p < 0.001$).

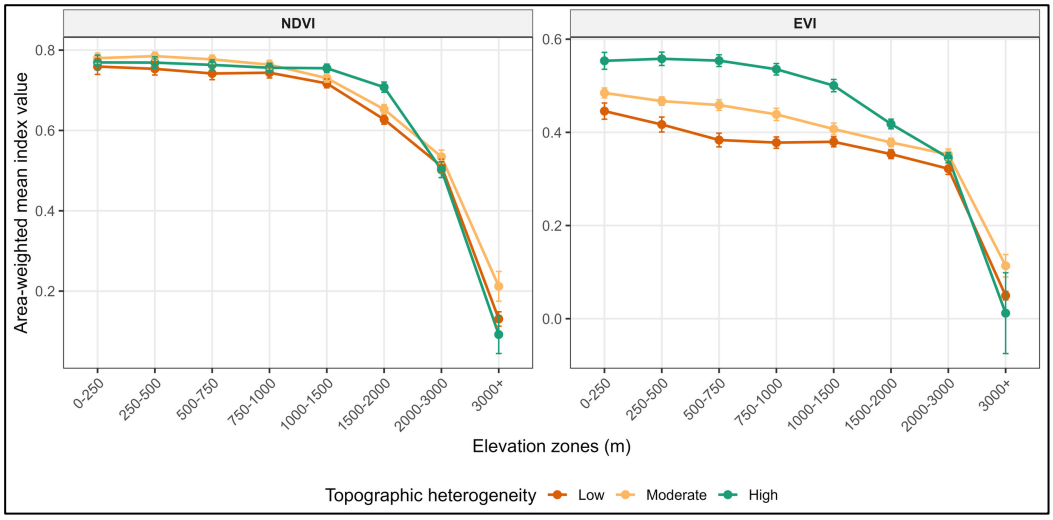


Figure 7. Area-weighted vegetation productivity across elevation and topographic heterogeneity classes. Area-weighted annual growing-season NDVI and EVI means are shown across elevation zones for low, moderate, and high topographic heterogeneity classes. Error bars indicate 95% confidence intervals



Figure 8. Area-weighted long-term NDVI and EVI dynamics across topographic heterogeneity classes. Annual growing-season area-weighted NDVI and EVI means are shown for low, moderate, and high topographic heterogeneity classes from 1985 to 2025. Solid lines and points represent annual values, and dashed lines represent linear trends

NDVI trends: The moderate TH class had the strongest trend (linear slope = 0.00469 year^{-1}; R^2 = 0.8331; Mann–Kendall τ = 0.7463; Sen slope = 0.00464, 95% CI 0.00407–0.00527). Low and high TH had linear slopes of 0.00422 and 0.00378 year^{-1}, respectively. High TH nevertheless maintained higher absolute NDVI than low TH through most of the record.

EVI trends: The moderate TH class again showed the largest increase (linear slope = 0.00334 year^{-1}; R^2 = 0.8257; Sen slope = 0.00327, 95% CI 0.00281–0.00385). Low and high TH had linear slopes of 0.00291 and 0.00296 year^{-1}. High TH occupied the highest absolute EVI level across nearly all years.

Table 1. Area-weighted long-term NDVI and EVI trend statistics across topographic heterogeneity classes

Index	Heterogeneity class	N years	Linear slope	Linear R^2	Mann–Kendall τ	Sen slope	95% CI for Sen slope	p-value
NDVI	Low	41	0.00422	0.7407	0.6537	0.00435	0.00342–0.00511	<0.001
	Moderate	41	0.00469	0.8331	0.7463	0.00464	0.00407–0.00527	<0.001
	High	41	0.00378	0.7950	0.6878	0.00377	0.00317–0.00443	<0.001
EVI	Low	41	0.00291	0.6455	0.6122	0.00293	0.00215–0.00374	<0.001
	Moderate	41	0.00334	0.8257	0.7341	0.00327	0.00281–0.00385	<0.001
	High	41	0.00296	0.7027	0.5951	0.00280	0.00223–0.00350	<0.001

3.6. Interannual stability and anomaly variability across heterogeneity classes

Area-weighted vegetation stability metrics exhibited a systematic response to the TH gradient, although the magnitude of this response varied between indices and metrics (Figure 9).

NDVI Stability: For NDVI, both temporal and interannual variability decreased monotonically as terrain complexity increased. The area-weighted mean temporal coefficient of variation (CV) declined from 10.29% in the low TH class to 9.44% in the moderate class and reached a minimum of 8.04% in the high TH class. A consistent pattern was observed for interannual anomaly variability; the anomaly standard deviation (SD) decreased from 0.0656 (low) to 0.0568 (high), while the mean absolute anomaly values similarly dropped from 0.0532 to 0.0461 along the same gradient.

EVI Stability: In the case of EVI, the temporal CV showed the most pronounced response to terrain structure, decreasing from 14.57% in low-heterogeneity areas to 10.71% in high-heterogeneity areas. However, unlike NDVI, EVI-based anomaly metrics remained relatively stationary across the heterogeneity classes. The mean anomaly SD showed negligible differences, with values of 0.0538 (low), 0.0530 (moderate), and 0.0529 (high). Mean absolute anomalies were also tightly clustered between 0.0422 and 0.0427 across all TH categories.

Overall, the results indicate that high topographic heterogeneity is associated with lower relative temporal variability (CV) for both indices, whereas the reduction in absolute interannual anomaly variability was index-specific, being clearly evident for NDVI but not for EVI.

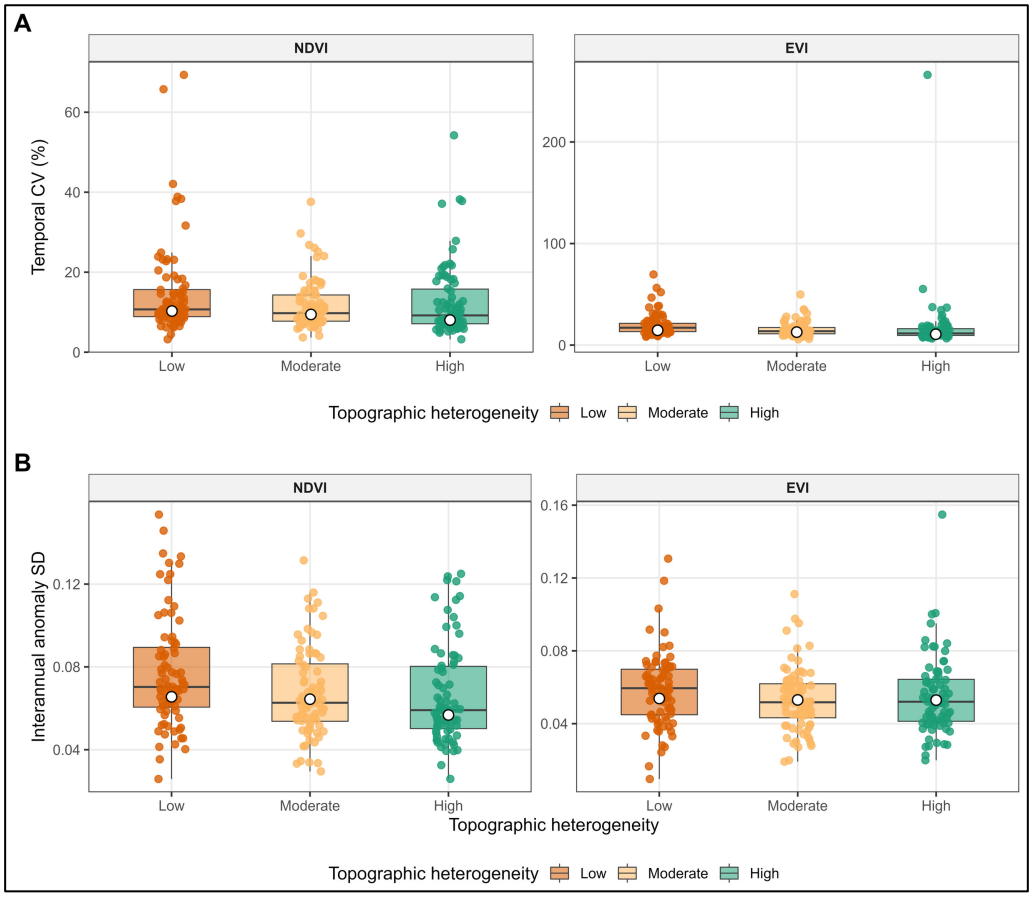


Figure 9. Area-weighted vegetation stability across topographic heterogeneity classes. (A) Temporal coefficient of variation calculated from annual growing-season means for land-cover-by-elevation-by-heterogeneity units. (B) Interannual anomaly variability expressed as anomaly standard deviation. White points indicate area-weighted class means

3.7. Area-weighted climate sensitivity to regional moisture forcing

After class-specific temporal trends were included and inference was clustered by year, current-year PDSI was not independently associated with NDVI or EVI anomalies. In the common 1986–2024 sample, current-year PDSI × TH interactions were non-significant for NDVI ($p = 0.643$) and EVI ($p = 0.629$). Model comparison instead supported a one-year-lagged PDSI formulation: it had the lowest AIC and BIC for EVI and the lowest BIC for NDVI.

NDVI lagged response: Previous-year PDSI slopes differed among TH classes (joint CR2 Wald $p = 0.0065$), but none of the individual class slopes was distinguishable from zero: low $\beta = -0.00379$ (95% CI −0.00882 to 0.00123; $p = 0.126$), moderate $\beta = 0.00020$ (95% CI −0.00372 to 0.00411; $p = 0.914$), and high $\beta = -0.00081$ (95% CI −0.00443 to 0.00281; $p = 0.636$). Thus, the NDVI result indicates heterogeneous slope structure rather than a confirmed lagged effect within a specific class.

EVI lagged response: The previous-year PDSI × TH interaction was significant (joint CR2 Wald $p = 0.0015$). Low TH showed a negative slope ($\beta = -0.00524$; CR2 standard error (SE) = 0.00189; 95% CI −0.00935 to −0.00113; $p = 0.0167$), whereas moderate ($\beta = -0.00177$; $p = 0.251$) and high TH ($\beta = -0.00141$; $p = 0.405$) were non-significant (Table 2). The pattern remained under quadratic and spline time controls, with the low-TH EVI slope significant in all three specifications and the interaction $p \leq 0.00017$ in the two nonlinear specifications.

The results do not support a uniform same-year negative PDSI effect. Instead, they indicate a heterogeneous, one-year-lagged association, strongest for EVI in low-heterogeneity terrain. Its negative sign is treated as an association rather than evidence that moisture deficit enhances vegetation (Figure 10).

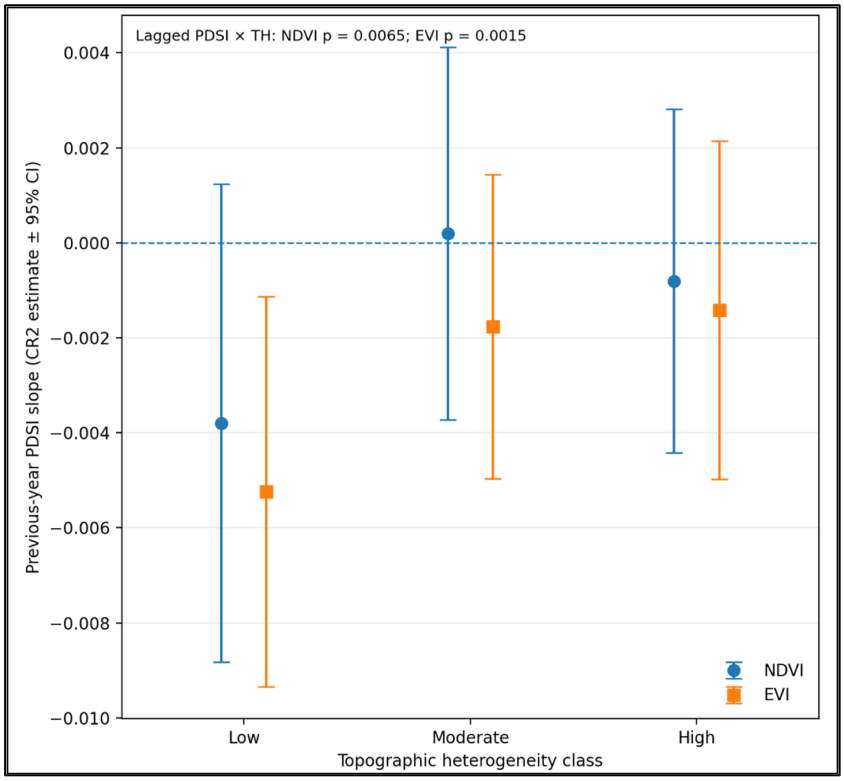


Figure 10. Year-clustered CR2 estimates of previous-year PDSI slopes for NDVI and EVI across topographic heterogeneity classes. Error bars are 95% confidence intervals. The horizontal dashed line indicates zero

Table 2. Previous-year PDSI slopes from the primary area-weighted, trend-controlled model with CR2 inference clustered by year

Index	Heterogeneity class	Lag-1 PDSI slope	CR2 SE	95% CI	t-ratio	p-value
NDVI	Low	−0.00379	0.00231	−0.00882 to 0.00123	−1.642	0.126
	Moderate	0.00020	0.00179	−0.00372 to 0.00411	0.110	0.914
	High	−0.00081	0.00166	−0.00443 to 0.00281	−0.486	0.636
EVI	Low	−0.00524	0.00189	−0.00935 to −0.00113	−2.776	0.0167
	Moderate	−0.00177	0.00146	−0.00497 to 0.00143	−1.210	0.251
	High	−0.00141	0.00164	−0.00498 to 0.00215	−0.863	0.405

Note. Models included class-specific linear time trends, elevation, and land cover and were weighted by valid analysis area. CR2 standard errors were clustered by year. Joint previous-year PDSI × TH tests were significant for NDVI (p = 0.0065) and EVI (p = 0.0015); only the low-TH EVI slope was individually significant.

3.8. Ecosystem stability metrics during extreme drought events

Four independent drought events were selected from the lowest 10% of growing-season PDSI (1994, 2014, 2018, and 2021). Drought-year deviations from class-specific linear trends varied in sign among events and did not show a uniform vegetation decline (Figure 11). Mean trend-adjusted drought-year deviations ranged from −1.27% to 0.84% for EVI and from −0.15% to 1.00% for NDVI across TH classes.

NDVI response: Trend-adjusted resistance was close to 1 in all classes (1.010 low, 1.008 moderate, and 0.999 high). Mean recovery ranged from 1.006 to 1.029, and mean resilience ranged from 1.015 to 1.039. These values describe modest post-event gains relative to fitted long-term trajectories rather than a statistically tested universal recovery response.

EVI response: Trend-adjusted resistance was 1.001 in low TH and slightly below 1 in moderate (0.985) and high TH (0.977). Recovery was 1.034–1.050 and resilience was 1.019–

1.050. Relative to raw metrics, linear detrending reduced mean resilience by 0.016–0.024, confirming that long-term greening inflated the unadjusted ratios but did not reverse their direction. Quadratic and spline detrending yielded the same directional conclusions (Table 3).

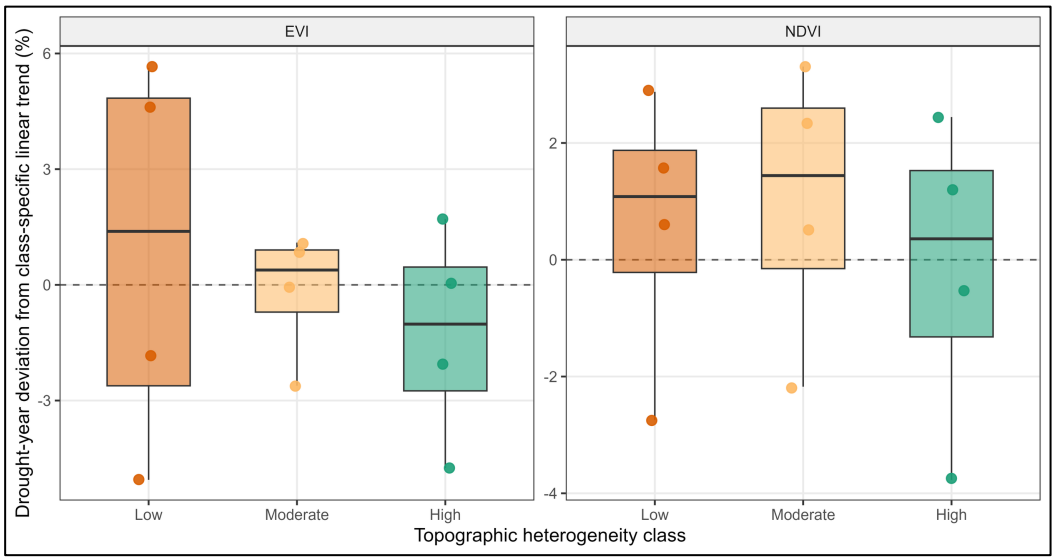


Figure 11. Drought-year NDVI and EVI deviations from class-specific linear trends across topographic heterogeneity classes. Points represent the four selected PDSI events; boxplots summarize event-to-event variation. The dashed line indicates no deviation from the fitted temporal trend

Table 3. Trend-adjusted drought resistance, recovery, and resilience metrics across topographic heterogeneity classes

Index	Heterogeneity class	N events	Pre-event mean	Drought-year mean	Post-event mean	Resistance	Recovery	Resilience
NDVI	Low	4	0.9970	1.0057	1.0346	1.010 ± 0.051	1.029 ± 0.036	1.039 ± 0.065
	Moderate	4	1.0021	1.0100	1.0159	1.008 ± 0.025	1.006 ± 0.028	1.015 ± 0.038
	High	4	0.9999	0.9985	1.0169	0.999 ± 0.025	1.019 ± 0.034	1.017 ± 0.030
EVI	Low	4	1.0106	1.0084	1.0577	1.001 ± 0.099	1.050 ± 0.038	1.050 ± 0.091
	Moderate	4	1.0149	0.9981	1.0321	0.985 ± 0.053	1.034 ± 0.016	1.019 ± 0.055
	High	4	1.0118	0.9873	1.0357	0.977 ± 0.051	1.050 ± 0.035	1.025 ± 0.035

Note. Values are based on annual indices divided by class-specific linear temporal trends. Resistance = drought-year/pre-event mean; recovery = post-event/drought-year mean; resilience = post-event/pre-event mean. Values are mean ± SD across four events and are interpreted descriptively. Quadratic and spline detrending produced the same directions.

3.9. Stratified bootstrap validation of productivity differences

A stratified bootstrap analysis (1000 iterations) was conducted to validate the robustness of the productivity gap between high and low topographic heterogeneity classes after matching for year, elevation, and land-cover strata (Figure 12).

NDVI Robustness: For NDVI, the observed area-weighted High–Low difference was 0.01264, with a nearly identical bootstrap mean of 0.01263. The 95% bootstrap confidence interval (0.00944–0.01576) remained entirely above the zero-difference threshold, yielding a probability of a positive difference of 1.000 ($p < 0.001$). Although the difference was statistically significant, the paired effect size was relatively small (Cohen's d = 0.221; partial $\eta^2 = 0.1700$). The area-weighted percentage of positive High–Low pairs was 61.9%.

EVI robustness: The observed High–Low difference was 0.11021 (bootstrap mean 0.11022), with a 95% interval of 0.10630–0.11410 entirely above zero (Figure 12). The

paired effect size was large (Cohen's d = 1.423; partial η^2 = 0.4384), and 92.3% of area-weighted pairs were positive.

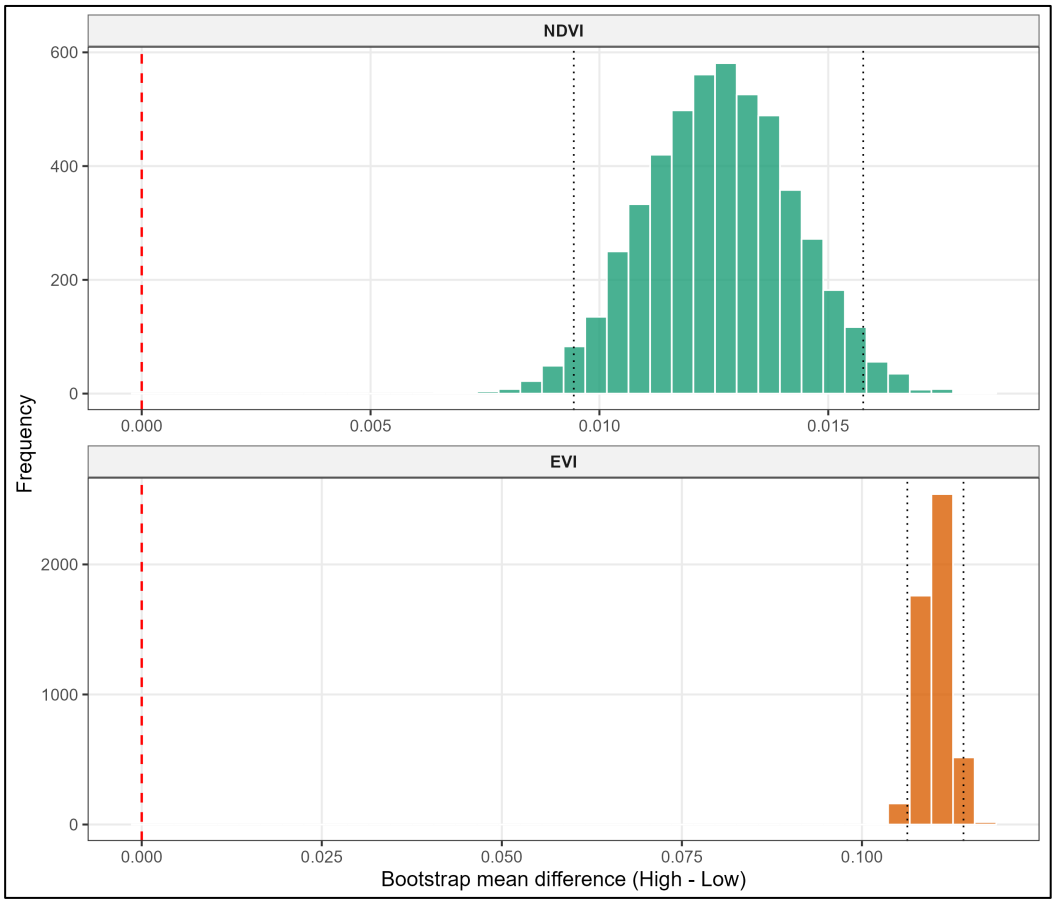


Figure 12. Area-weighted bootstrap robustness of High–Low productivity differences. Bootstrap distributions of mean High–Low differences for NDVI and EVI. Differences were calculated within matched year × elevation × land-cover strata. The red dashed line indicates zero difference, and black dotted lines indicate the 95% bootstrap confidence interval

3.10. Raster-scale sensitivity of topographic heterogeneity classes

The original 5 m class raster was independently aggregated by majority class to 30 m and 100 m. Coarse cells were retained when at least 50% of their underlying 5 m cells were valid. At 30 m, overall agreement with the original map was 77.51% (Cohen's κ = 0.586), with mean class purity of 0.775. At 100 m, agreement declined to 72.03% (κ = 0.468) and mean purity to 0.720 (Table 4).

Aggregation increased the moderate class from 59.35% at 5 m to 64.88% at 30 m and 69.34% at 100 m, while reducing the relative area of both low and high TH. Thus, the broad spatial organization remained recognizable at Landsat scale, but progressively coarser grids smoothed the most contrasting terrain classes. This analysis evaluates classification stability only and does not rerun the NDVI/EVI models.

Table 4. Raster-scale sensitivity of the three-class topographic heterogeneity map

Scale (m)	Low (%)	Moderate (%)	High (%)	Agreement (%)	Cohen's κ	Mean purity
5	18.88	59.35	21.77	100.00	1.000	1.000
30	15.30	64.88	19.82	77.51	0.586	0.775
100	12.46	69.34	18.21	72.03	0.468	0.720

Note. Original values were regrouped as low = 0–1, moderate = 2, and high = 3–5. Coarse classes were defined by the majority of valid 5 m cells; at least 50% valid coverage was required.

4. Discussion

4.1. Topographic heterogeneity as a multidimensional control of vegetation productivity

The spatial correspondence between high THI values and high vegetation productivity zones (Figure 4) suggests that multidimensional terrain complexity provides an important physiographic template for vegetation development in Trabzon Province. The representative field photographs (Figure 4d–f) provide ground-level context for this pattern, illustrating incised valleys, rugged hillslopes, exposed rock surfaces, and heterogeneous vegetation structures within the marked high-complexity area. These landform conditions may enhance local moisture retention, topographic shading, and microclimatic buffering, thereby creating more favorable vegetation conditions than those found on less complex surrounding slopes. This aligns with integrated assessments in other rugged landscapes, where topography and aspect orientation have been shown to function as essential microclimatic refugia, effectively protecting vegetation health and moisture levels from regional environmental stressors (Dhammar et al., 2026).

This study demonstrates that topographic heterogeneity is associated with systematic differences in long-term vegetation productivity in a humid mountainous landscape. The high topographic heterogeneity class generally exhibited higher area-weighted NDVI and EVI values than the low heterogeneity class, even when vegetation summaries were structured by land-cover class and elevation zone. This finding supports the central expectation that terrain complexity is not merely a passive background condition, but a spatial filter that can differentiate vegetation productivity within the same regional climatic setting (Muscarella et al., 2020).

The result is consistent with recent work emphasizing that topography can structure vegetation dynamics through its control over radiation, water redistribution, and microclimatic variation. For example, global Landsat-based evidence from alpine zones shows that topographic conditions modulate both vegetation greening and vegetation area expansion, and that elevation and aspect can produce divergent vegetation-change patterns across mountainous regions (Zou et al., 2025). Similarly, recent vegetation–topography coupling research in the Loess Plateau indicates that topographic heterogeneity can shape spatial heterogeneity in vegetation status, particularly through its influence on water availability, solar radiation, and landform-controlled environmental conditions (Luo et al., 2024). Our study extends this logic to a humid mountain environment by using a multi-layer Shannon entropy-based topographic heterogeneity index rather than a single topographic variable.

The stronger separation observed for EVI than for NDVI is also ecologically meaningful. EVI is generally more responsive to canopy structural variation in dense or high-biomass vegetation, while NDVI can become less sensitive when canopy greenness is already high. This helps explain why the High–Low difference was much larger for EVI than for NDVI and why the bootstrap analysis showed a stronger effect size for EVI. The implication is not that NDVI is unsuitable, but that NDVI and EVI capture partly different dimensions of vegetation condition in a humid, densely vegetated mountain landscape. In this context, EVI appears more sensitive to heterogeneity-related differences in canopy condition, whereas NDVI provides a more conservative greenness signal (Stein et al., 2014).

The elevation-stratified results further indicate that the effect of topographic heterogeneity is not uniform across the elevation gradient. The 1000–2000 m elevation interval broadly overlaps the transition from mixed broadleaved–conifer forests to conifer-dominated montane forests in the Eastern Black Sea region, whereas subalpine and alpine vegetation becomes prevalent above the regional treeline at approximately 2000 m (Atalay, 2002). Consequently, part of the elevation-dependent variation in NDVI and EVI among TH classes may reflect covariation between terrain configuration and altitudinal vegetation

zonation rather than an entirely independent effect of topographic heterogeneity. Although the elevation- and land-cover-stratified analyses reduce this potential confounding, they cannot eliminate it completely.

Differences among heterogeneity classes were more pronounced at low and middle elevations and diminished above 2000 m, suggesting that the ecological expression of topographic heterogeneity depends on its position along the elevation gradient. At higher elevations, temperature limitation, shorter growing seasons, reduced soil development, and greater exposure may override local heterogeneity effects (Rogora et al., 2018). This situation is consistent with broader mountain research showing that topographic controls interact with elevation-dependent climatic constraints rather than operating independently. Global evidence from alpine regions further indicates that the influence of topography on vegetation dynamics varies among vegetation metrics and along elevation gradients, reinforcing the need to assess topographic effects within an elevation-stratified framework rather than as a single landscape-wide relationship (Zou et al., 2025).

4.2. Long-term greening and stability across heterogeneity classes

The long-term NDVI and EVI results indicate a clear greening signal from 1985 to 2025 across all topographic heterogeneity classes. This suggests that the study area has experienced a broad increase in growing-season vegetation greenness and canopy condition over the last four decades. However, the trend magnitudes were not highest in the high heterogeneity class. Instead, the moderate heterogeneity class showed the strongest NDVI and EVI trend magnitudes, while the high heterogeneity class generally maintained higher absolute index values across much of the time series.

This distinction is important. Higher topographic heterogeneity was associated more clearly with higher productivity levels than with the fastest rate of increase. In other words, high heterogeneity areas appear to occupy a relatively high-productivity state through time, whereas moderate heterogeneity areas showed stronger upward trends. This may reflect the fact that high heterogeneity zones already supported relatively high vegetation index values earlier in the record, leaving less room for strong additional increases (Piao et al., 2020). It may also indicate that moderate heterogeneity landscapes provide enough environmental variability to support greening while still retaining larger areas of climatically or physiographically favorable vegetation units.

The stability results provide an additional dimension to this interpretation. Temporal coefficient of variation decreased from low to high heterogeneity classes for both NDVI and EVI, and NDVI anomaly variability was also lower in the high heterogeneity class. These patterns support the idea that heterogeneous terrain can reduce temporal variability in vegetation condition, likely because local variation in slope, aspect, radiation exposure, moisture accumulation, and landform position creates a broader range of microsites. Such microsite diversity may allow different parts of the landscape to respond differently to annual climatic variability, reducing the overall variability of the aggregated vegetation signal (S. Wang & Loreau, 2014).

This interpretation aligns with the growing microclimate literature showing that fine-scale topographic variation can create local climatic conditions that are decoupled from broader macroclimatic forcing. Recent empirical work demonstrates that microrefugia can maintain distinct temperature and vapor pressure deficit conditions during extreme events, potentially reducing plant water stress (Finocchiaro et al., 2024). Similarly, topography-driven microclimate gradients have been shown to influence forest structure, diversity, and composition in refugial forest systems, indicating that small-scale terrain variation can have persistent ecological consequences (McNichol et al., 2024). Our results do not directly measure microclimate, but they are consistent with the expectation that terrain heterogeneity may contribute to more stable vegetation-index behavior through spatial averaging of contrasting local responses.

At the same time, the stability signal was stronger for temporal CV than for anomaly-based EVI metrics. This means that the conclusion should be framed carefully: high heterogeneity areas showed lower relative temporal variability, but not all stability metrics responded equally. The study therefore supports a nuanced interpretation in which topographic heterogeneity contributes to vegetation stability, especially in NDVI and CV-based metrics, but does not uniformly reduce all forms of interannual variability.

4.3. Hydroclimatic sensitivity and drought-year responses: evidence and caution

The hydroclimatic analysis indicates that the apparent same-year negative PDSI relationships largely reflect opposing long-term trends: PDSI declined through time while NDVI and EVI increased. After accounting for class-specific time trends and year-level dependence, current-year PDSI effects and interactions were not supported. The results instead indicate a heterogeneous one-year-lagged association (Schwalm et al., 2017).

The lagged EVI association was concentrated in low TH, whereas moderate and high TH slopes were weak and non-significant. This attenuation is compatible with, but does not prove, topographic buffering: contrasting aspects, slope positions, shading, fog interception, and soil-water redistribution may reduce the correspondence between a regional moisture index and local canopy conditions (De Frenne et al., 2021). The negative low-TH slope remains ecologically counterintuitive and may reflect delayed phenology, radiation-cloud covariation, unmeasured disturbance, or residual temporal confounding. It is therefore interpreted as a robust statistical association rather than a causal benefit of drought.

NDVI and EVI differed in inferential detail. NDVI showed significant heterogeneity among lagged slopes, but no class-specific slope differed from zero. EVI showed both a significant interaction and an individually significant low-TH slope. This difference is plausible because EVI is more sensitive to canopy structure and high-biomass variation, whereas NDVI saturates more readily in dense vegetation (Xue & Su, 2017). Accordingly, the climate result is index-specific and should not be generalized as a common vegetation response.

The trend-adjusted drought analysis further showed that regional PDSI extremes did not generate a consistent drought-year decline. Recovery and resilience ratios remained above 1 on average, but only four independent events were available and error bars represent event-to-event SD rather than inferential confidence intervals. Detrending reduced the magnitude of post-event ratios, demonstrating that part of the raw apparent resilience reflected background greening. These metrics are therefore descriptive event summaries, not evidence of statistically universal ecosystem recovery (Buras et al., 2020).

Future hydroclimatic analyses should combine PDSI with locally responsive indicators. Candidate alternatives include the Standardized Runoff Index (SRI) for hydrological drought, the Vegetation Condition Index (VCI) and Temperature Condition Index (TCI) for satellite-observed vegetation and thermal stress, and direct soil-moisture, vapor-pressure-deficit, fog/cloud-frequency, and radiation data. Such combinations would help distinguish moisture limitation from radiation or temperature limitation in humid mountain environments.

4.4. Methodological contribution, scale sensitivity, and limitations

The principal contribution is a multidimensional, entropy-based representation of terrain structure linked to four decades of vegetation observations. Equal weighting preserves transparent contributions from 11 standardized terrain dimensions and avoids allowing sample-specific variance to determine ecological importance. Nevertheless, it assumes equal relevance and ignores covariance; PCA-weighted or expert-weighted alternatives should be tested where the original continuous entropy layers and independent validation data are available (Gan et al., 2017).

The independent scale analysis provides a direct assessment of classification uncertainty. Agreement remained 77.5% when the 5 m map was generalized to 30 m,

supporting broad compatibility with Landsat-scale patterns, but κ was moderate rather than near-perfect. At 100 m, increased dominance of the moderate class showed that CORINE-scale integration smooths fine terrain contrasts. CORINE should therefore be understood as a broad categorical control, not as fine-resolution land-cover information.

Several limitations remain. First, NDVI and EVI are proxies affected by canopy structure, background reflectance, atmosphere, and illumination geometry; terrain shadow and cloud contamination may persist despite compositing and median summaries (Ma et al., 2024). Second, the archived THI has 5 m output spacing, but the provenance and native accuracy of the source DEM were not retained. The study therefore does not equate 5 m cell spacing with 5 m elevation accuracy.

Third, the available processing records do not document the exact GEE resampling settings. The retained extraction table confirms grouped land-cover × elevation × TH units and areas based on 30 m Landsat pixel counts. The raster-scale sensitivity analysis partly addresses this uncertainty, but it does not substitute for rerunning the complete vegetation workflow at multiple grids.

Fourth, aggregation into ecological units reduces pixel-level pseudo-replication but does not eliminate spatial dependence. The retained analytical dataset contains no coordinates, grid identifiers, or geometries, so a valid residual Moran's I test could not be reconstructed. Applying Moran's I to the TH raster itself would not test model residuals and was therefore avoided. The CR2 year clustering addresses temporal dependence in the regional PDSI models, but spatial uncertainty remains; future implementations should retain georeferenced block identifiers for residual diagnostics, spatial block bootstrap, or spatial mixed models.

Finally, microclimatic buffering was inferred rather than measured. The higher productivity and lower relative variability of high TH can arise because mosaics of aspect, slope position, shading, soil depth, and moisture redistribution create asynchronous local responses that stabilize an area-weighted signal. At high elevations, however, short growing seasons, low temperature, exposure, and weak soil development impose regional constraints that can override this microsite diversity, explaining the observed convergence among TH classes.

Despite these limitations, the convergence of area-weighted productivity comparisons, elevation stratification, long-term stability metrics, matched-strata bootstrap results, and 30 m raster sensitivity supports a consistent association between terrain complexity and vegetation condition. The framework is transferable, provided future studies preserve full terrain provenance, processing scripts, and georeferenced analytical units.

5. Conclusions

This study answers the first research question by showing that high topographic heterogeneity is associated with higher long-term NDVI and especially EVI after stratification by elevation and land cover. The difference was strongest below 2000 m, weakened at higher elevations, and remained positive in matched-strata bootstrap analyses.

For the second research question, all TH classes greened during 1985–2025, but moderate TH showed the largest rate of increase, whereas high TH maintained higher absolute productivity and lower relative temporal variability. Thus, terrain complexity was linked more strongly to productive state and stability than to maximum greening rate.

For the third research question, current-year PDSI effects were not supported after temporal-trend and dependence corrections. Previous-year PDSI responses differed among TH classes, with a significant negative EVI association only in low TH; drought-event responses were variable and descriptive. The 30 m scale analysis preserved the broad TH pattern, whereas 100 m aggregation smoothed the extreme classes. The conclusions should therefore be interpreted as robust landscape associations, not direct proof of microclimatic or causal drought mechanisms.

Acknowledgments: The author thanks the editor and anonymous reviewers for their constructive comments, which led to substantial methodological clarification and additional robustness analyses. The author also acknowledges technical assistance received during the original Google Earth Engine data extraction.

Author Contributions: The author confirms sole responsibility for the following: study conception and design, data collection, analysis and interpretation of results, and manuscript preparation.

AI Contribution Statement: ChatGPT (OpenAI, GPT-5) was used for English language editing and code troubleshooting. All scientific analyses, results, interpretations, and references were independently reviewed, verified, and approved by the author.

Funding: This study received no external funding.

Research and publication ethics statement: The author declares that there is no violation of research and publication ethics. The study did not involve human participants or animals and did not require ethics committee approval.

Conflicts of Interest: The author declares no conflicts of interest.

Data Availability: The analytical tables, revision scripts, and raster-scale sensitivity outputs are available from the corresponding author upon reasonable request.

Abbreviations:
The following abbreviations are used in this manuscript:

CORINE	Coordination of Information on the Environment
CR2	Cluster-Robust Variance Estimator
DEM	Digital Elevation Model
EVI	Enhanced Vegetation Index
GEE	Google Earth Engine
NDVI	Normalized Difference Vegetation Index
PDSI	Palmer Drought Severity Index
SRTM	Shuttle Radar Topography Mission
TH	Topographic Heterogeneity
THI	Topographic Heterogeneity Index

References

Abatzoglou, J. T., Dobrowski, S. Z., Parks, S. A., & Hegewisch, K. C. (2018). TerraClimate, a high-resolution global dataset of monthly climate and climatic water balance from 1958–2015. *Scientific Data*, 5(1), 170191. https://doi.org/10.1038/sdata.2017.191

Aktaş, C. (2024). Google Earth Engine ve MODIS tabanlı NDVI verileri ile Aras Nehri yukarı kesiminde bitki örtüsü üzerindeki ekim ayı değişimlerinin incelenmesi (2001–2022) [Investigation of October changes in vegetation cover in the upper reaches of the Aras River using Google Earth Engine and MODIS-based NDVI data (2001–2022)]. *Journal of Anatolian Geography*, 1(2), 108–120.

Atalay, İ. (2002). *Türkiye'nin ekolojik bölgeleri*. Orman Bakanlığı yayınları.

Bueno de Mesquita, C. P., Tillmann, L. S., Bernard, C. D., Rosemond, K. C., Molotch, N. P., & Suding, K. N. (2018). Topographic heterogeneity explains patterns of vegetation response to climate change (1972–2008) across a mountain landscape, Niwot Ridge, Colorado. *Arctic, Antarctic, and Alpine Research*, 50(1), e1504492. https://doi.org/10.1080/15230430.2018.1504492

Buras, A., Rammig, A., & Zang, C. S. (2020). Quantifying impacts of the 2018 drought on European ecosystems in comparison to 2003. *Biogeosciences*, 17(6), 1655–1672. https://doi.org/10.5194/bg-17-1655-2020

Büttner, G. (2014). CORINE Land Cover and Land Cover Change Products. In I. Manakos & M. Braun (Eds.), *Land use and land cover mapping in Europe: Practices & trends* (pp. 55–74). Springer Netherlands. https://doi.org/10.1007/978-94-007-7969-3_5

Conrad, O., Bechtel, B., Bock, M., Dietrich, H., Fischer, E., Gerlitz, L., Wehberg, J., Wichmann, V., & Böhner, J. (2015). System for Automated Geoscientific Analyses (SAGA) v. 2.1.4. *Geoscientific Model Development*, 8(7), 1991–2007. https://doi.org/10.5194/gmd-8-1991-2015

De Frenne, P., Lenoir, J., Luoto, M., Scheffers, B. R., Zellweger, F., Aalto, J., Ashcroft, M. B., Christiansen, D. M., Decocq, G., De Pauw, K., Govaert, S., Greiser, C., Gril, E., Hampe, A., Jucker, T., Klinges, D. H., Koelemeijer, I. A., Lembrechts, J. J., Marrec, R., … Hylander, K. (2021). Forest microclimates and climate change: Importance, drivers and future research agenda. *Global Change Biology*, 27(11), 2279–2297. https://doi.org/10.1111/gcb.15569

Dhammar, R., Odedra, K., & Jadeja, B. A. (2026). Integrated geo-hydro-biological assessment of Barda Hills: Vegetation dynamics, land surface temperature trends, and conservation strategies (1995–2025). *Turkish Journal of Remote Sensing*, 8, 1–29. https://doi.org/10.51489/tuzal.1734764

Efron, B., & Tibshirani, R. J. (1994). *An Introduction to the Bootstrap*. Chapman & Hall/CRC. https://doi.org/10.1201/9780429246593

Eraslan, B. (2024). Topografyanın insan modifikasyonu üzerindeki etkisi: Doğu ve Orta Karadeniz örneği [The impact of topography on human modification: The case of Eastern and Central Black Sea]. *Journal of Anatolian Geography*, 1(1), 51–61.

Farr, T. G., Rosen, P. A., Caro, E., Crippen, R., Duren, R., Hensley, S., Kobrick, M., Paller, M., Rodriguez, E., Roth, L., Seal, D., Shaffer, S., Shimada, J., Umland, J., Werner, M., Oskin, M., Burbank, D., & Alsdorf, D. (2007). The Shuttle Radar Topography Mission. *Reviews of Geophysics*, 45(2). https://doi.org/10.1029/2005RG000183

Finocchiaro, M., Médail, F., Saatkamp, A., Diadema, K., Pavon, D., Brousset, L., & Meineri, E. (2024). Microrefugia and microclimate: Unraveling decoupling potential and resistance to heatwaves. *Science of the Total Environment*, 924, 171696. https://doi.org/10.1016/j.scitotenv.2024.171696

Flood, N. (2013). Seasonal composite Landsat TM/ETM+ images using the medoid (a multi-dimensional median). *Remote Sensing*, 5(12), 6481–6500. https://doi.org/10.3390/rs5126481

Gan, X., Fernandez, I. C., Guo, J., Wilson, M., Zhao, Y., Zhou, B., & Wu, J. (2017). When to use what: Methods for weighting and aggregating sustainability indicators. *Ecological Indicators*, 81, 491–502. https://doi.org/10.1016/j.ecolind.2017.05.068

Gorelick, N., Hancher, M., Dixon, M., Ilyushchenko, S., Thau, D., & Moore, R. (2017). Google Earth Engine: Planetary-scale geospatial analysis for everyone. *Remote Sensing of Environment*, 202, 18–27. https://doi.org/10.1016/j.rse.2017.06.031

Gürçay, B., Köse, N., & Avcı, M. (2025). Dendroclimatological analyses in a protected area and its surroundings: A case study of the Örümcek Forest. *Dendrobiology*, 93, 69–85. https://doi.org/10.12657/denbio.093.005

Huete, A., Didan, K., Miura, T., Rodriguez, E. P., Gao, X., & Ferreira, L. G. (2002). Overview of the radiometric and biophysical performance of the MODIS vegetation indices. *Remote Sensing of Environment*, 83(1–2), 195–213. https://doi.org/10.1016/S0034-4257(02)00096-2

Ibarra-Manríquez, G., González-Espinosa, M., Martínez-Ramos, M., & Meave, J. A. (2022). From vegetation ecology to vegetation science: Current trends and perspectives. *Botanical Sciences*, 100(Special Issue), S137–S174. https://doi.org/10.17129/botsci.3171

Işık, F., Bahadır, M., Zeybek, H. İ., & Hatipoğlu, İ. K. (2024). Elevation-dependent growth trends of *Picea orientalis* (L.) Peterm. forests in the Fırtına Creek Basin (Rize/Turkey). *Dendrobiology*, 91, 56–69. https://doi.org/10.12657/denbio.091.005

Işık, F., & Eraslan, S. (2026). Multi-scale greening dynamics in Türkiye's Ecoregions (2001–2024): The effects of elevation and land cover on NDVI change tendencies. *Environmental Monitoring and Assessment*, 198(4), 323. https://doi.org/10.1007/s10661-026-15173-9

Kaya, Z., & Raynal, D. J. (2001). Biodiversity and conservation of Turkish forests. *Biological Conservation*, 97(2), 131–141. https://doi.org/10.1016/S0006-3207(00)00069-0

Liang, T., Tian, F., Zou, L., Jin, H., Tagesson, T., Rumpf, S., He, T., Liang, S., & Fensholt, R. (2024). Global assessment of vegetation patterns along topographic gradients. *International Journal of Digital Earth*, 17(1), 2404232. https://doi.org/10.1080/17538947.2024.2404232

Luo, Z., Liu, Y., & Zhou, H. (2024). The vegetation–topography heterogeneity coupling in the Loess Plateau, China. *Frontiers in Environmental Science*, 12, 1343215. https://doi.org/10.3389/fenvs.2024.1343215

Ma, Y., He, T., McVicar, T. R., Liang, S., Liu, T., Peng, W., Song, D.-X., & Tian, F. (2024). Quantifying how topography impacts vegetation indices at various spatial and temporal scales. *Remote Sensing of Environment*, 312, 114311. https://doi.org/10.1016/j.rse.2024.114311

Mann, H. B. (1945). Nonparametric tests against trend. *Econometrica*, 13(3), 245–259. https://doi.org/10.2307/1907187

Masek, J. G., Wulder, M. A., Markham, B., McCorkel, J., Crawford, C. J., Storey, J., & Jenstrom, D. T. (2020). Landsat 9: Empowering open science and applications through continuity. *Remote Sensing of Environment*, 248, 111968. https://doi.org/10.1016/j.rse.2020.111968

McNichol, B. H., Wang, R., Hefner, A., Helzer, C., McMahon, S. M., & Russo, S. E. (2024). Topography-driven microclimate gradients shape forest structure, diversity, and composition in a temperate refugial forest. *Plant-Environment Interactions*, 5(3), e10153. https://doi.org/10.1002/pei3.10153

Moeslund, J. E., Arge, L., Bøcher, P. K., Dalgaard, T., & Svenning, J.-C. (2013). Topography as a driver of local terrestrial vascular plant diversity patterns. *Nordic Journal of Botany*, 31(2), 129–144. https://doi.org/10.1111/j.1756-1051.2013.00082.x

Muscarella, R., Kolyaie, S., Morton, D. C., Zimmerman, J. K., & Uriarte, M. (2020). Effects of topography on tropical forest structure depend on climate context. *Journal of Ecology,* 108(1), 145–159. https://doi.org/10.1111/1365-2745.13261

Öztürk, M. Z., Çetinkaya, G., & Aydın, S. (2017). Köppen-Geiger iklim sınıflandırmasına göre Türkiye'nin iklim tipleri [Climate types of Turkey according to Köppen-Geiger climate classification]. *Journal of Geography*, *(*35*)*, 17–27. https://doi.org/10.26650/JGEOG295515

Piao, S., Wang, X., Park, T., Chen, C., Lian, X., He, Y., Bjerke, J. W., Chen, A., Ciais, P., Tømmervik, H., Nemani, R. R., & Myneni, R. B. (2020). Characteristics, drivers and feedbacks of global greening. *Nature Reviews Earth & Environment*, 1(1), 14–27. https://doi.org/10.1038/s43017-019-0001-x

R Core Team. (2022). *R: A language and environment for statistical computing* [Computer software]. R Foundation for Statistical Computing. https://www.R-project.org/

Riley, S. J., DeGloria, S. D., & Elliot, R. (1999). A terrain ruggedness index that quantifies topographic heterogeneity. *Intermountain Journal of Sciences*, 5(1), 23–27.

Rogora, M., Frate, L., Carranza, M. L., Freppaz, M., Stanisci, A., Bertani, I., Bottarin, R., Brambilla, A., Canullo, R., Carbognani, M., Cerrato, C., Chelli, S., Cremonese, E., Cutini, M., Di Musciano, M., Erschbamer, B., Godone, D., Iocchi, M., Isabellon, M., … Matteucci, G. (2018). Assessment of climate change effects on mountain ecosystems through a cross-site analysis in the Alps and Apennines. *Science of the Total Environment*, 624, 1429–1442. https://doi.org/10.1016/j.scitotenv.2017.12.155

Schwalm, C. R., Anderegg, W. R. L., Michalak, A. M., Fisher, J. B., Biondi, F., Koch, G., Litvak, M., Ogle, K., Shaw, J. D., Wolf, A., Huntzinger, D. N., Schaefer, K., Cook, R., Wei, Y., Fang, Y., Hayes, D., Huang, M., Jain, A., & Tian, H. (2017). Global patterns of drought recovery. *Nature*, 548(7666), 202–205. https://doi.org/10.1038/nature23021

Şekercioğlu, Ç. H., Anderson, S., Akçay, E., Bilgin, R., Can, Ö. E., Semiz, G., Tavşanoğlu, Ç., Yokeş, M. B., Soyumert, A., İpekdal, K., Sağlam, İ. K., Yücel, M., & Dalfes, H. N. (2011). Turkey's globally important biodiversity in crisis. *Biological Conservation*, 144(12), 2752–2769. https://doi.org/10.1016/j.biocon.2011.06.025

Sen, P. K. (1968). Estimates of the regression coefficient based on Kendall's tau. *Journal of the American Statistical Association*, 63(324), 1379–1389. https://doi.org/10.1080/01621459.1968.10480934

Shannon, C. E. (1948). A mathematical theory of communication. *Bell System Technical Journal*, 27(3), 379–423. https://doi.org/10.1002/j.1538-7305.1948.tb01338.x

Stein, A., Gerstner, K., & Kreft, H. (2014). Environmental heterogeneity as a universal driver of species richness across taxa, biomes and spatial scales. *Ecology Letters*, 17(7), 866–880. https://doi.org/10.1111/ele.12277

Sturtevant, B. R., & Fortin, M.-J. (2021). Understanding and modeling forest disturbance interactions at the landscape level. *Frontiers in Ecology and Evolution*, 9, 653647. https://doi.org/10.3389/fevo.2021.653647

Suggitt, A. J., Wilson, R. J., Isaac, N. J. B., Beale, C. M., Auffret, A. G., August, T., Bennie, J. J., Crick, H. Q. P., Duffield, S., Fox, R., Hopkins, J. J., Macgregor, N. A., Morecroft, M. D., Walker, K. J., & Maclean, I. M. D. (2018). Extinction risk from climate change is reduced by microclimatic buffering. *Nature Climate Change*, 8(8), 713–717. https://doi.org/10.1038/s41558-018-0231-9

Torresani, M., Rossi, C., Perrone, M., Hauser, L. T., Féret, J.-B., Moudrý, V., Šímová, P., Ricotta, C., Foody, G. M., Kacic, P., Feilhauer, H., Malavasi, M., Tognetti, R., & Rocchini, D. (2024). Reviewing the spectral variation hypothesis: Twenty years in the tumultuous sea of biodiversity estimation by remote sensing. *Ecological Informatics*, 82, 102702. https://doi.org/10.1016/j.ecoinf.2024.102702

Tucker, C. J. (1979). Red and photographic infrared linear combinations for monitoring vegetation. *Remote Sensing of Environment*, 8(2), 127–150. https://doi.org/10.1016/0034-4257(79)90013-0

Wang, C., & Zhao, H. (2018). Spatial heterogeneity analysis: Introducing a new form of spatial entropy. *Entropy*, 20(6), 398. https://doi.org/10.3390/e20060398

Wang, J., Liu, H., Yang, Q., Shen, G., Zhu, X., Xu, Y., & Wang, X. (2023). Topography and structural diversity regulate ecosystem multifunctionality in a subtropical evergreen broad-leaved forest. *Frontiers in Forests and Global Change*, 6, 1309660. https://doi.org/10.3389/ffgc.2023.1309660

Wang, S., & Loreau, M. (2014). Ecosystem stability in space: α, β and γ variability. *Ecology Letters*, 17(8), 891–901. https://doi.org/10.1111/ele.12292

Wani, Z. A., Negi, V. S., Bhat, J. A., Satish, K. V., Kumar, A., Khan, S., Dhyani, R., Siddiqui, S., Al-Qthanin, R. N., & Pant, S. (2023). Elevation, aspect, and habitat heterogeneity determine plant diversity and compositional patterns in the Kashmir Himalaya. *Frontiers in Forests and Global Change*, 6, 1019277. https://doi.org/10.3389/ffgc.2023.1019277

Weiss, A. D. (2001). *Topographic Position and Landforms Analysis* [Conference poster]. ESRI International User Conference, San Diego, CA, United States.

White, M. A., de Beurs, K. M., Didan, K., Inouye, D. W., Richardson, A. D., Jensen, O. P., O'Keefe, J., Zhang, G., Nemani, R. R., van Leeuwen, W. J. D., Brown, J. F., de Wit, A., Schaepman, M., Lin, X., Dettinger, M., Bailey, A. S., Kimball, J., Schwartz, M. D., Baldocchi, D. D., … Lauenroth, W. K. (2009). Intercomparison, interpretation, and assessment of spring phenology in North America estimated from remote sensing for 1982–2006. *Global Change Biology*, 15(10), 2335–2359. https://doi.org/10.1111/j.1365-2486.2009.01910.x

Xu, Y., Franklin, S. B., Wang, Q., Shi, Z., Luo, Y., Lu, Z., Zhang, J., Qiao, X., & Jiang, M. (2015). Topographic and biotic factors determine forest biomass spatial distribution in a subtropical mountain moist forest. *Forest Ecology and Management*, 357, 95–103. https://doi.org/10.1016/j.foreco.2015.08.010

Xue, J., & Su, B. (2017). Significant remote sensing vegetation indices: A review of developments and applications. *Journal of Sensors*, 2017(1), 1353691. https://doi.org/10.1155/2017/1353691

Zou, L., Tian, F., Liang, T., Fensholt, R., He, T., & Schaepman-Strub, G. (2025). Topographic effects on vegetation greening and area expansion in global alpine zones under climate change. *International Journal of Applied Earth Observation and Geoinformation*, 142, 104727. https://doi.org/10.1016/j.jag.2025.104727